CHARACTERISTICS OF NEAR-FAULT ACCELERATION PULSES AND IMPLICATIONS ON THE BUILDING STRUCTURES

Z. Chang[(1)], F. De Luca[(2)], K. Goda[(3)]

[(1)] *Assistant Professor, Southwest Jiaotong University, zhiwang_chang@163.com*
[(2)] *Senior Lecturer, University of Bristol, flavia.deluca@bristol.ac.uk*
[(3)] *Associate Professor, Western University, kgoda2@uwo.ca*

Abstract

Ground motions with strong velocity pulses are of particular concern among structural engineers. Historical evidence shows that the velocity pulses can be further grouped into either a distinct acceleration-pulse (acc-pulse) or a succession of high-frequency, one-sided acceleration spikes (non-acc-pulse). This study introduces a new algorithm that can be used to automatically distinguish the pulse-like features of the two types of velocity pulses. The algorithm is then used to compile a ground motion dataset which consists of 74 acc-pulses and 45 non-acc-pulses. An energy-based parameter, the MEA/MEV ratio, is proposed for characterizing the properties of pulse-like records. Here, 'MEA' and 'MEV' represent the Maximum Energy of the half-cycle pulse in Acceleration and Velocity time histories, respectively. Finally, the influences of acc-pulses and non-acc-pulses on the inelastic displacement ratio (C_R) spectra are studied. Results indicate that the characteristics of the two types of velocity pulses differ significantly, leading to clearly distinct C_R spectral properties. The findings of this study stress the importance of distinguishing different velocity pulses when it comes to the selection of near-fault ground motions for evaluating the nonlinear seismic response of structures. It is shown in this study that the MEA/MEV ratio can characterize the spectral shapes of near-fault ground motions better than PGA/PGV, and its use can improve the estimation of the C_R spectra.

Keywords: near-fault; velocity pulse; acceleration pulse; inelastic displacement ratio

1. Introduction

Strong ground motions with velocity pulses are of special interest among seismologists and earthquake engineers. Largely impacted by the forward-directivity effects or the fling-step effects[1], these motions are expected to impose particularly high seismic demands on structures. During the last two decades, the near-fault pulse-like ground motion has been an active research subject in seismology and earthquake engineering. Historical evidence from previous events, such as the 1994 Northridge earthquake [2], shows that flexible structures may experience severe nonlinear behavior or even partial or complete collapse if the pulse period (T_p) of a record is close to the fundamental vibration period (T) of a structure.

In the past studies [3–5], further classifications of pulse-like ground motions, beyond the characterization of velocity pulses, are rarely discussed and largely overlooked. In fact, the velocity pulse can be further categorized into either a distinct acceleration pulse (acc-pulse) or a succession of high-frequency, one-sided acceleration spikes (non-acc-pulse) [6,7]. For illustration, two example ground motions, recorded during the 1979 Coyote Lake earthquake and the 1992 Landers earthquake, are shown in Fig. 1. Dominant pulses can be identified by visually inspecting the velocity time-histories of the two records. By examining their acceleration time-histories more carefully, it can be observed that the two dominant velocity pulses contain significantly different frequency content. Specifically, in Fig. 1a, the velocity pulse is the integral of a distinct low-frequency acc-pulse; while in Fig. 1b the velocity pulse is a result of a series of high-frequency, one-sided spikes. The velocity pulses having different frequency content can cause different effects on the structures. A local acc-pulse, such as the Coyote Lake example in Fig. 1a, is more damaging to structures with short-to-moderate periods (1.5-2.5s); while a non-acc-pulse, such as the Landers example in Fig. 1b, has significant impacts on the long-period structures (>4s) [8].

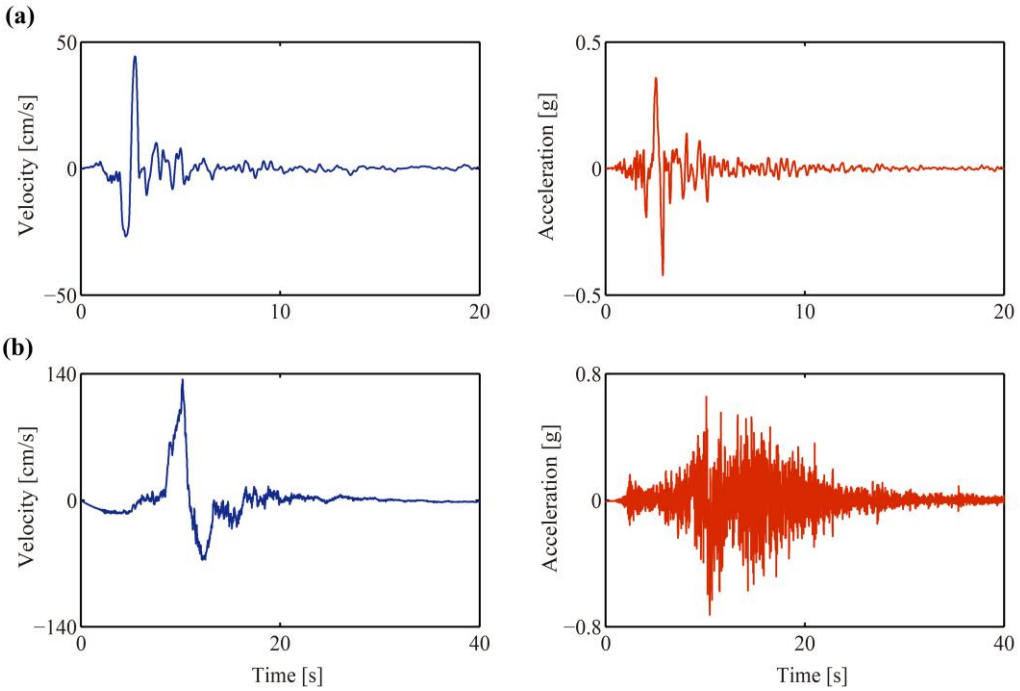

Fig. 1-Velocity and acceleration time histories for: (a) a ground motion containing both velocity and acceleration pulse, (b) a ground motion with velocity pulse but without acceleration pulse. The first motion is the G06230 component (RSN150) recorded in the 1979 Coyote Lake earthquake; the second is the LCN260 component (RSN879) recorded in the 1992 Landers earthquake.

Despite the potential differences of seismic demands resulting from the two different types of velocity pulses, investigations on this topic are limited, except for a few pioneer studies. No systematic statistical analyses have been carried out. In this regard, a new algorithm for automatically classifying acc-pulses and non-acc-pulses can be implemented to reveal how the velocity pulses of different characteristics may affect the inelastic response of structures. This study introduces a new algorithm that can be used to automatically distinguish the pulse-like features of the two types of velocity pulses. The algorithm is then employed to compile a ground motion dataset which consists of 74 acc-pulses and 45 non-acc-pulses. An energy-based parameter, the MEA/MEV ratio, is proposed for characterizing the properties of pulse-like records. Here, 'MEA' and 'MEV' represent the Maximum Energy of the half-cycle pulse in Acceleration and Velocity time histories, respectively. Finally, the influences of acc-pulses and non-acc-pulses on the inelastic displacement ratio (C_R) spectra are studied. Prior studies indicated that the PGA/PGV ratio is a suitable parameter for representing the combined effects of earthquake magnitude, faulting mechanism, distance to fault, and soil conditions. It is shown in this study that the MEA/MEV ratio can characterize the spectral shapes of near-fault ground motions better than PGA/PGV, and thus its use can improve the estimation of the C_R spectra.

2. Algorithm for classifying acceleration pulses and non-acceleration pulses

The classification of acceleration pulses is performed using the algorithm by Chang et al.[9]. It uses the wavelet packets transform (WPT) for filtering the high-frequency content and the peak-point-method for determining the pulse-starting and -ending time instants (t_s and t_e). The energy of the velocity pulse (EVP) and the energy of the acceleration pulse (EAP) are then calculated and employed as the indicator for identifying the pulse-like features in the velocity and acceleration time histories, respectively. This automated approach is outlined in the following steps, and a graphical flowchart is summarized in Fig. 2.

1) Determination of the pulse-starting and -ending time instants:

Use the WPT to remove the high-frequency content by retaining the top wavelet packet coefficients (WPCs) that account for 70% of the total WPCs, while setting all remaining WPCs to zeroes. Reconstruct the

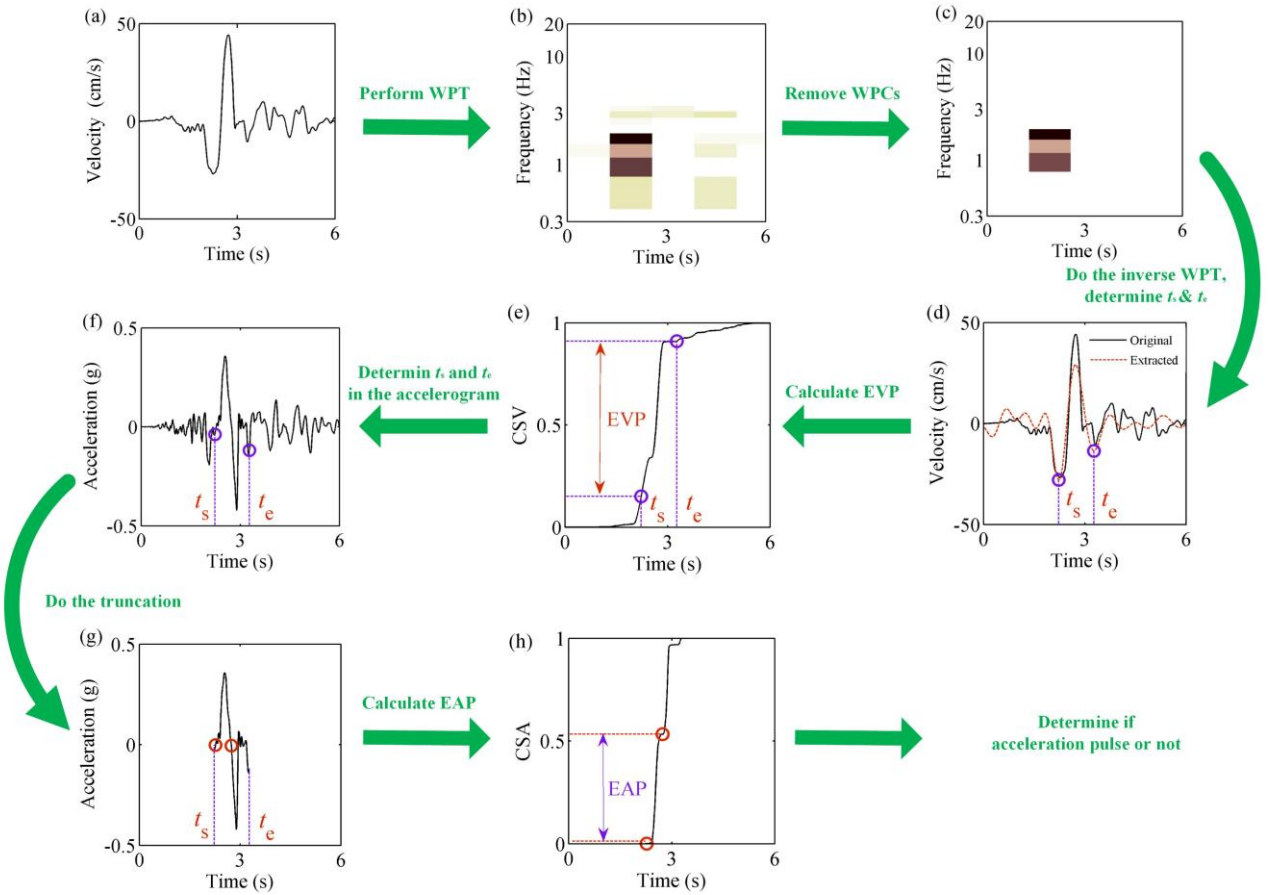

Fig. 2 -Flowchart of the approach for classifying acc-pulses and non-acc-pulses (adapted from [9]).

main velocity pulse by applying the inverse-WPT to the top WPCs. Determine the t_s and t_e according to the peak-point-method (PPM). The time interval between t_s and t_e is used for representing the pulse period of T_p.

2) Calculation of EVP

Calculate the relative cumulative squared velocities (CSV) as well as the relative energy of the velocity pulse (EVP) with respect to the original velocity time-history. EVP is expressed as follows:

$$\mathrm{EVP} = \mathrm{CSV}(t_e) - \mathrm{CSV}(t_s) = \frac{\int_0^{t_e} v^2(\tau)\,d\tau}{\int_0^{D} v^2(\tau)\,d\tau} - \frac{\int_0^{t_s} v^2(\tau)\,d\tau}{\int_0^{D} v^2(\tau)\,d\tau}, \quad (1)$$

where D indicates the total duration of the ground motion; $v(t)$ represents the velocity time series. When the EVP is larger than 0.35, significant velocity pulse features can be detected.

3) Extraction of the acceleration time-history

For ground motions with EVP larger than 0.35, a local acceleration time-history is then extracted using t_s and t_e.

4) Calculation of EAP and classification of the acceleration pulses

With the extracted acceleration time-history, all zero-crossings are identified. The cumulative squared accelerations (CSA) as well as the energy of the acc-pulse (EAP) between every two adjacent zero-crossings are calculated. EAP is formulated as:

$$\mathrm{EAP} = \mathrm{CSA}(t_2)\text{-}\mathrm{CSA}(t_1) = \frac{\int_{t_s}^{t_2} a^2(\tau)\,d\tau}{\int_{t_s}^{t_e} a^2(\tau)\,d\tau} - \frac{\int_{t_s}^{t_1} a^2(\tau)\,d\tau}{\int_{t_s}^{t_e} a^2(\tau)\,d\tau}, \tag{2}$$

where t_1 and t_2 are the time-starting and -ending time instants of the half-cycle pulse; and $a(t)$ indicates the acceleration time series of the extracted ground motion. The maximum EAP is used as the indicator for classifying acc-pulses. When the EAP is smaller than 0.25, the record is classified as non-acc-pulse; when it is larger than 0.50, the record is classified as acc-pulse.

To systematically analyze the different characteristics of acc-pulses and non-acc-pulses, the above algorithm is applied to an expanded ground motion dataset, and 74 acc-pulses and 45 non-acc-pulses are identified (see the Appendix table for further information). These 119 ground motions were recorded in 28 historical earthquake events with M_w ranging from 5.74 to 7.62. A map view of the geographical distribution of the earthquake epicenters is illustrated in Fig. 3, and detailed information regarding these pulse-like records is listed in the Appendix. It should be noted that these 119 components are all considered as early-arriving pulses and are potentially caused by forward-directivity effects.

3. Proposed ground motion measure: MEA/MEV

The mathematical expression for the MEA/MEV ratio is as follows [10]:

$$\frac{\mathrm{MEA}}{\mathrm{MEV}}(\mathrm{Hz}) = \left(\frac{\int_{t_{as}}^{t_{ae}} a^2(t)\,\mathrm{dt}}{\int_{t_{vs}}^{t_{ve}} v^2(t)\,\mathrm{dt}} \right)^{0.5} \tag{3}$$

where $a(t)$ and $v(t)$ represents the acceleration value and the velocity value at time t, respectively. t_{as} and t_{ae} are the starting and ending time instants of the half-cycle acceleration pulse having the energy; t_{vs} and t_{ve} are the starting and ending time instants of the half-cycle pulse in the velocity time history, respectively.

The G06230 component (RSN150) recorded in the 1979 Coyote Lake earthquake is used for illustration in Fig. 4a and 4b. To compute MEA, all zero-crossing time instants are first identified, and the time integrals of squared accelerations between the two adjacent zero-crossing time instants are evaluated. The largest integral is then determined as MEA. Physically, MEA corresponds to the half-cycle pulse having

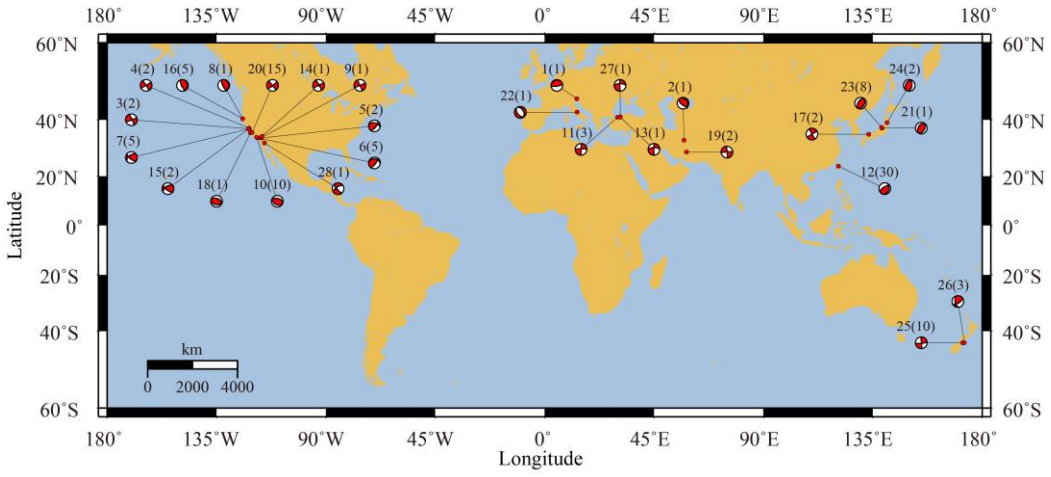

Fig. 3 -Map view of the geographical distribution of earthquake epicenters together with the so-called beach-ball diagrams to show the mechanisms of the fault rupture for the ground motions used in this study. The numbers outside the brackets represent the earthquake ID (EQID) in Appendix, while those inside the brackets are the number of ground motions for each event.

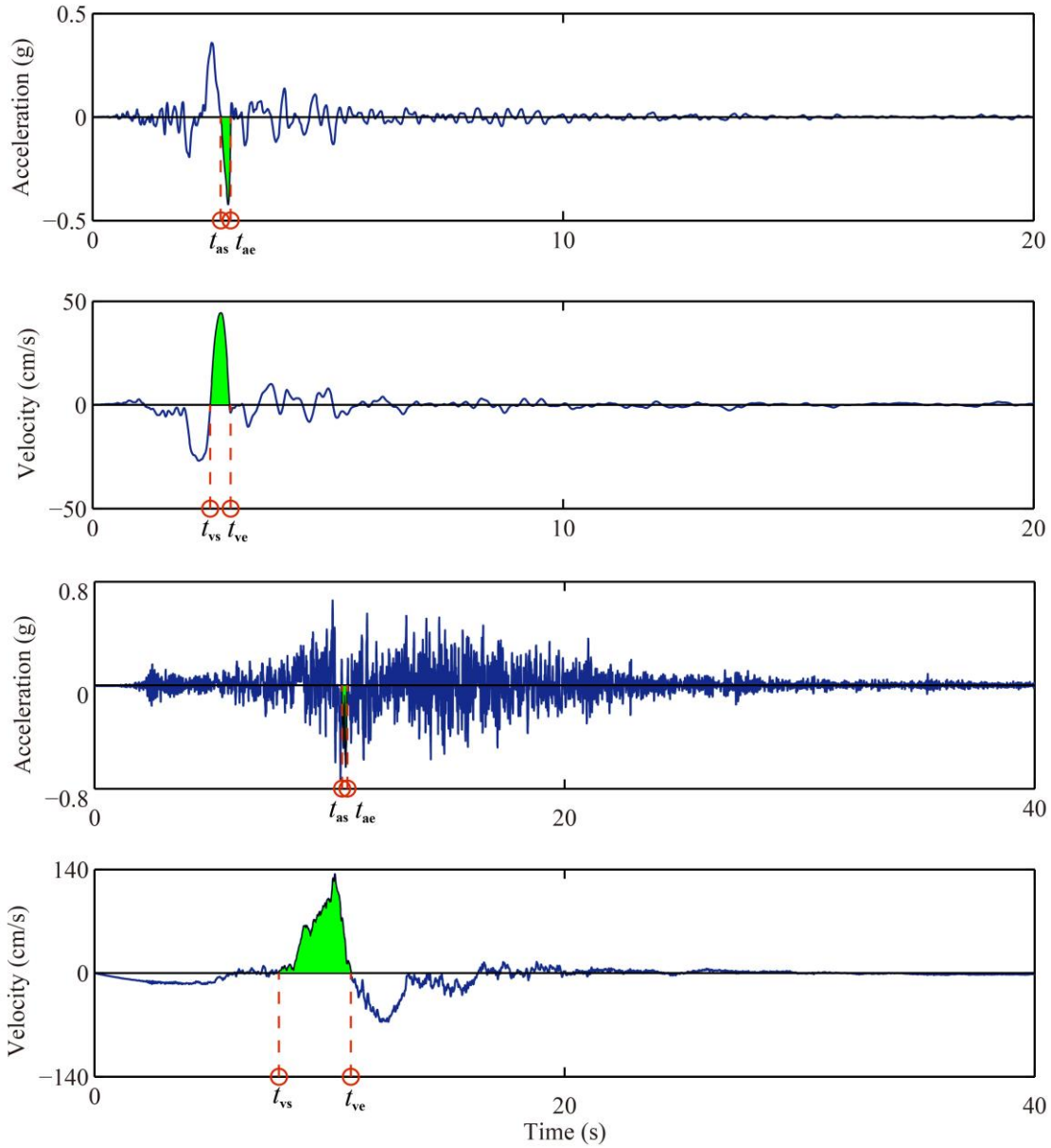

Fig. 4 -Acceleration (a) and velocity (b) time histories of the G06230 component (RSN150) recorded in the 1979 Coyote Lake earthquake; acceleration (c) and velocity (d) time histories of the LCN260 component (RSN879) recorded in the 1992 Landers earthquake. MEA/MEV ratios of the two components are 6.5 and 1.3 Hz, respectively; PGA/PGV ratios of the two records are 9.3 and 5.3Hz, respectively.

the largest area enclosed by the horizontal axis and the accelerogram, see Fig. 4a. It represents the largest seismic energy concentrated within a half-cycle pulse. MEV is similar to MEA, and its computation is with respect to the velocity time histories, see Fig. 4b. The G06230 component is one of those records having a large MEA/MEV ratio, with its value reaching 6.5 Hz. A ground motion with a small MEA/MEV ratio is additionally shown in Fig. 4c and 4d. It comes from the LCN260 component (RSN879) which was recorded in the 1992 Landers earthquake, and has a MEA/MEV ratio of 1.3 Hz.

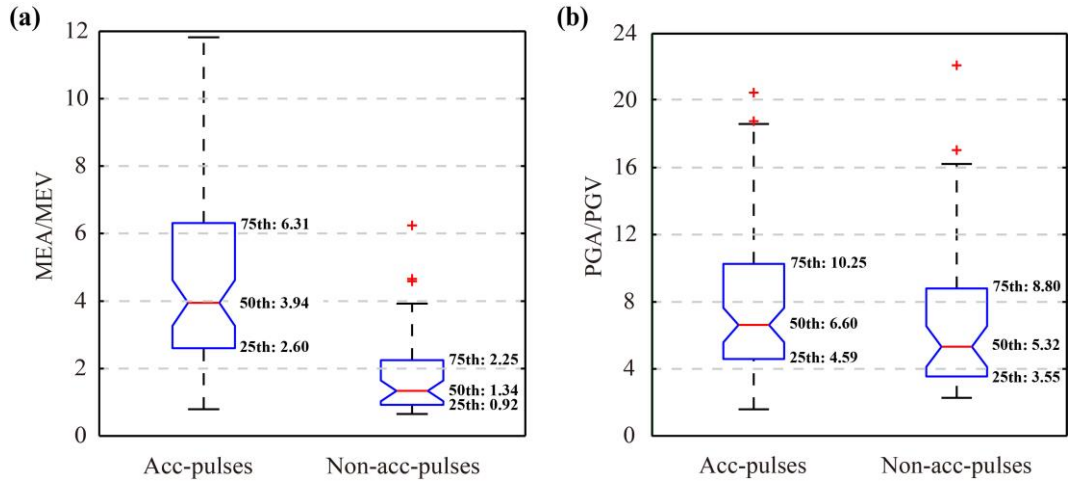

Fig. 5 -Boxplots for: (a) MEA/MEV and (b) PGA/PGV. In each boxplot, the central red line denotes the median of the data (50th percentile), and the edges of the box (blue lines) mark the 25th and 75th percentiles. The ends of the whiskers represent the extreme data points not considered outliers, while the symbols of red '+' are individual outliers.

To examine the relationship between the acc-pulses and the MEA/MEV ratios, the ground motions listed in Appendix are grouped into three sets according to the values of MEA/MEV. The boundary values for the grouping are manually determined so that the numbers of ground motions in the three sets are close to one another. Based on this criterion, the range for Set A is chosen as MEA/MEV<2.0, in which 38 ground motions are assigned; the range for Set B is 2.0≤ MEA/MEV≤ 5.0, in which there are 43 records; and the range for Set C is MEA/MEV>5.0, in which 38 records are allocated. The boxplots for the two types of velocity pulses, and the relevant distributions for MEA/MEV are illustrated in Fig. 5a. Generally, MEA/MEV for acc-pulses is much larger than that for non-acc-pulses. The median value (50th percentile) for acc-pulses is 3.94, which is almost three times larger than that for non-acc-pulses (i.e., 3.94>1.34); in addition, the 25th percentile of acc-pulses is found even larger than the 75th percentile of non-acc-pulses (i.e., 2.60>2.25). For comparison, similar distributions for PGA/PGV are displayed in Fig. 5b. It is clearly seen that the differences in PGA/PGV between the two groups of velocity pulses are not as significant as those for MEA/MEV, although overall PGA/PGV for acc-pulses is slightly larger than that for non-acc-pulses. The above observations indicate that MEA/MEV is better than PGA/PGV for distinguishing velocity pulses with different characteristics (i.e., acc-pulses versus non-acc-pulses).

The pulse period (T_p) is often used as an index to represent the frequency content of near-fault ground motions, and it is considered to be quite related to the earthquake source parameters, such as the earthquake magnitude M_w [3,9]. Then it is interesting to investigate the relation between T_p and MEA/MEV as well as PGA/PGV, see Fig. 6. The T_p values are calculated using the peak-point-method [4]. It is obvious in Fig. 6a that a strong correlation can be found between T_p and MEA/MEV, and their absolute correlation coefficient reaches 0.78. Whereas in Fig. 6b, the relationship between T_p and PGA/PGV is not as strong as that in Fig. 6a; the correlation coefficient is only 0.53. The stronger relation between T_p and MEA/MEV serves as another evidence that MEA/MEV can be a more desirable parameter than PGA/PGV in reflecting the properties of velocity pulses with different frequency content.

4. Influence of MEA/MEV on C_R

To examine the effect of hysteretic models on the C_R spectra under the three record sets, ratios of the C_R spectra for EPH, EPH-d, and EPH-dp systems to the C_R spectra for EPP systems are calculated for each R

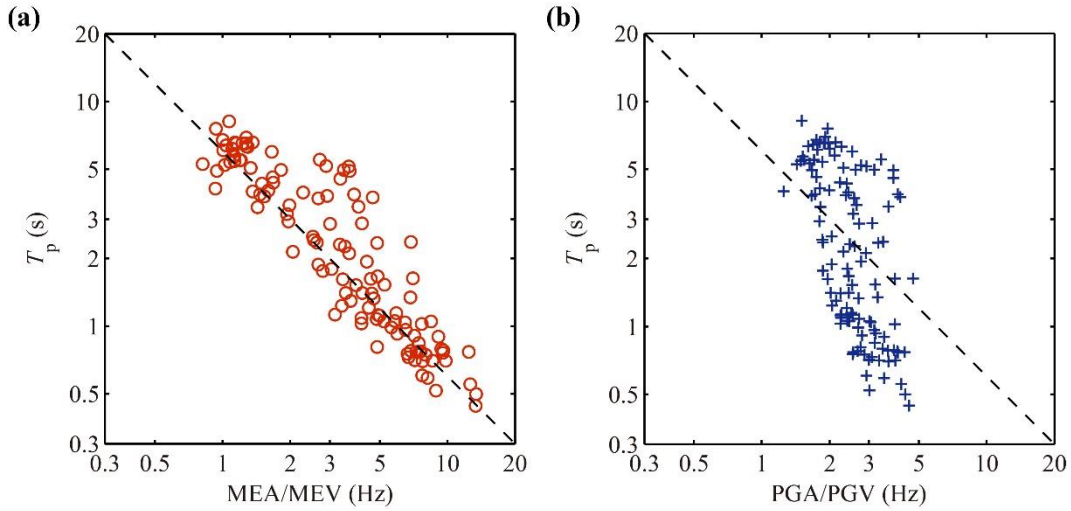

Fig. 6 -(a) Relationship between T_p and MEA/MEV; (b) relationship between T_p and PGA/PGV. The T_p values are computed by the peak-point-method in [9].

level; the mean ratios are displayed in Fig. 7. It is observed from the first two columns that within each record set, there are no significant differences between $C_{R,\,EPH}/C_{R,\,EPP}$ and $C_{R,\,EPH\text{-}d}/C_{R,\,EPP}$ (i.e., Fig. 7a vs 7b; Fig. 7d vs 7e; Fig. 7g vs 7h). The mean ratios within all three record sets become smaller as T decreases and as R increases. In the short-period range (T<1.0s), the mean ratio is generally smaller than 1.0, meaning that the C_R spectral values for the EPH and EPH-d systems are on average smaller than those for EPP systems. In the intermediate- to long-period ranges (T>1.0s), the mean ratio is close to 1.0, meaning that the C_R spectral values for the EPH and EPH-d systems can be approximated to those for EPP systems.

For records in Set A, the $C_{R,\,EPH\text{-}dp}/C_{R,\,EPP}$ ratios in Fig. 7c for high R-levels (i.e., R=4 and 6) are similar to those in Fig. 7a and 7b. On the other hand, the ratios for low R-levels (i.e., R=1.5 and 2) are significantly different. The mean ratio in the short-period range (T<1.0s) exhibits an inverted V-shape, and can exceed 1.0 significantly. This observation is consistent with the findings in Chang et al. [11] as the majority of the records in Set A is comprised of ground motions with non-acc-pulses. The trends of the $C_{R,\,EPH\text{-}dp}/C_{R,\,EPP}$ ratio for Set B in Fig. 7f is similar to those found in Fig. 7c, although the differences among different R-levels for the former are not as significant as those for the latter. For records in Set C, no pronounced differences are observed of the $C_{R,\,EPH\text{-}dp}/C_{R,\,EPP}$ ratio with respect to different R-levels and different hysteretic models, see Fig. 7i. Considering that most of the records in Set C are acc-pulses, it is concluded that for acc-pulses with low MEA/MEV values, the effects of hysteretic models on the C_R spectra are rather limited, and there are no major differences when the hysteretic models vary from EPH to EPH-dp.

5. Conclusions

A new algorithm is introduced to automatically distinguish the pulse-like features of the two types of velocity pulses. This algorithm is employed to to compile a ground motion dataset comprising 74 acc-pulses and 45 non-acc-pulses. An energy-based parameter, the MEA/MEV ratio, is proposed for characterizing the properties of pulse-like records. Finally, the influences of acc-pulses and non-acc-pulses on the inelastic displacement ratio (C_R) spectra are studied. It is indicated that the characteristics of the two types of velocity pulses differ significantly, causing clearly different C_R spectral properties. The significance of this study is to stress the importance of distinguishing different velocity pulses when selecting pulse-like ground motions for evaluating the nonlinear seismic response of structures in near-fault regions. It is shown in this study that the MEA/MEV ratio can characterize the spectral shapes of near-fault ground motions better than PGA/PGV, and its use can improve the estimation of the C_R spectra.

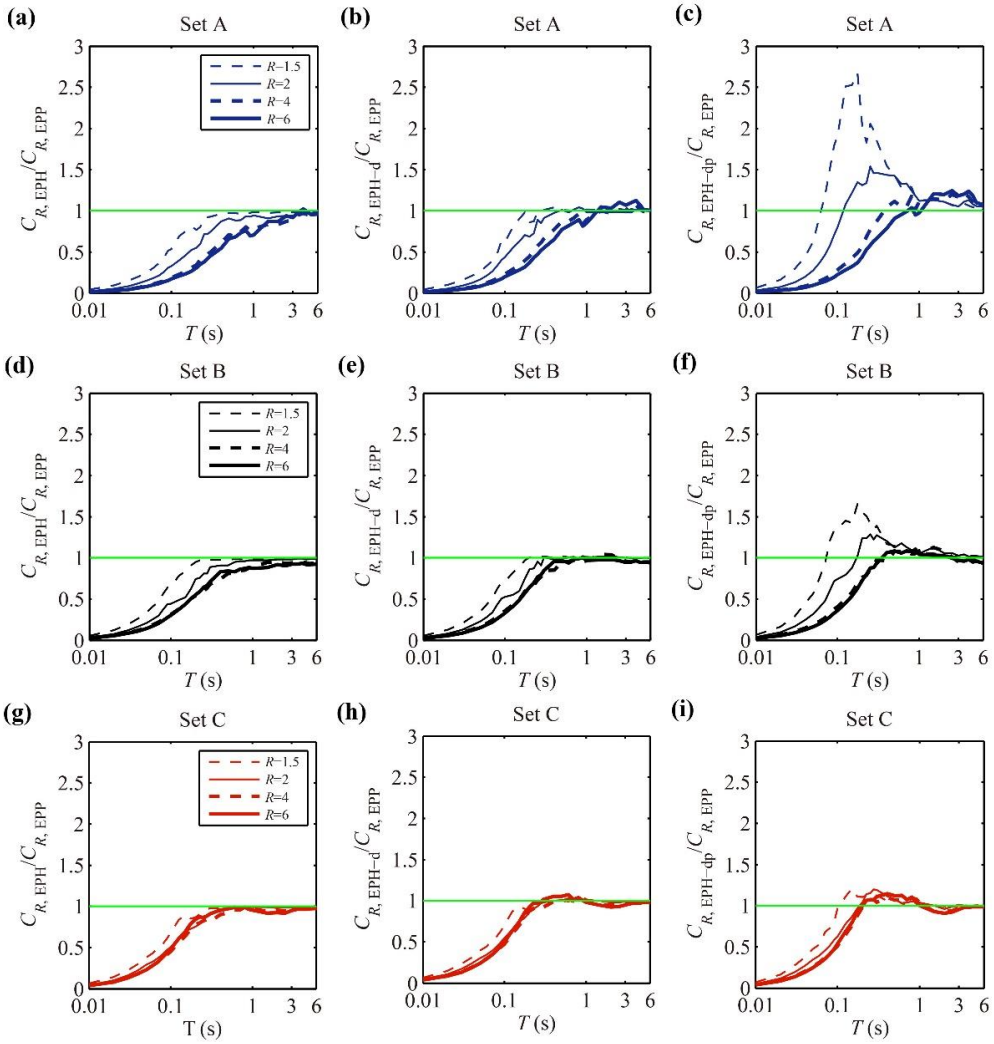

Fig. 7 -Effect of hysteretic models on the C_R spectra; top panels for record set A: (a) $C_{R,\,EPH}/C_{R,EPP}$; (b) $C_{R,EPH\text{-}d}/C_{R,EPP}$; (c) $C_{R,EPH\text{-}dp}/C_{R,EPP}$; medium panels for record set B: (d) $C_{R,\,EPH}/C_{R,EPP}$; (e) $C_{R,EPH\text{-}d}/C_{R,EPP}$; (f) $C_{R,EPH\text{-}dp}/C_{R,EPP}$; bottom panels for record set C: (g) $C_{R,\,EPH}/C_{R,EPP}$; (h) $C_{R,EPH\text{-}d}/C_{R,EPP}$; (i) $C_{R,EPH\text{-}dp}/C_{R,EPP}$.

6. References

[1] Kalkan E, Kunnath SK (2006): Effects of fling step and forward directivity on seismic response of buildings. *Earthquake Spectra*, **22**, 367-90.

[2] Hall JF, Heaton TH, Halling MW, Wald DJ (1995): Near-source ground motion and its effects on flexible buildings. *Earthquake Spectra*, **11**, 569-605.

[3] Baker JW (2007): Quantitative classification of near-fault ground motions using wavelet analysis. *Bulletin of Seismological Society of America*, **97**, 1486-1501.

[4] Zhai C, Chang Z, Li S, Chen Z, Xie L (2013): Quantitative identification of near-fault pulse-like ground motions based on energy. *Bulletin of Seismological Society of America*, **103**, 2591-2603.

[5] Chang Z, Sun X, Zhai C, Zhao JX, Xie L (2016): An improved energy-based approach for selecting pulse-like ground motions. *Earthquake Engineering & Structural Dynamics*, **45**, 2405-2411.

[6] Bertero V V., Mahin SA, Herrera RA (1978): Aseismic design implications of near−fault san fernando earthquake records. *Earthquake Engineering & Structural Dynamics*, **6**,31-42.

[7] Kalkan E, Kunnath SK (2008): Relevance of absolute and relative energy content in seismic evaluation of structures. *Advances in Structural Engineering*, **11**, 17-34.

[8] Makris N, Black CJ (2004): Evaluation of peak ground velocity as a "good" intensity measure for near-source ground motions. *Journal of Engineering Mechanics*,**130**:1032.

[9] Chang Z, De Luca F, Goda K (2019): Automated classification of near-fault acceleration pulses using wavelet packets. *Computer-aided Civil and Infrastructre Engineering*, **34**, 569-585.

[10] Chang Z, De Luca F, Goda K (2020): A new proxy for near-fault acceleration pulses and implications on inelastic displacement ratio. *Soil Dynamics and Earthquake Engineering*, (under review).

[11] Chang Z, De Luca F, Goda K (2019): Near-fault acceleration pulses and non-acceleration pulses: Effects on the inelastic displacement ratio. *Earthquake Engineering & Structural Dynamics*, **48**, 1256-1276.

Appendix

Table A1 Information of near-fault pulse-like ground motions used in this study

EQID	RSN	Earthquake Event	M_w	R_{rup} (km)	Component	PGA (g)	PGA/PGV (Hz)	MEA/MEV (Hz)	$T_{p,PPM}$ (s)
1	125	Friuli-01, Italy	6.5	15.8	TMZ000	0.67	15.3	7.7	1.0
2	143	Tabas, Iran	7.4	2.1	TAB-T1	0.06	6.8	1.8	5.0
3	149	Coyote Lake	5.7	5.7	G04360	0.24	7.7	7.1	0.9
3	150	Coyote Lake	5.7	3.1	G06230	0.21	9.3	6.5	1.0
4	451	Morgan Hill	6.2	0.5	CYC195	0.25	13.2	6.9	0.8
4	451	Morgan Hill	6.2	0.5	CYC285	0.21	16.3	9.6	0.8
5	529	N. Palm Springs	6.1	4.0	NPS210	0.16	10.3	6.0	0.9
5	540	N. Palm Springs	6.1	6.0	WWT180	0.32	12.2	9.2	0.9
6	614	Whittier, Narrows-01	6.0	20.8	A-BIR180	0.21	8.6	7.7	0.6
6	615	Whittier, Narrows-01	6.0	20.8	A-DWN180	0.21	6.5	7.3	0.8
6	615	Whittier, Narrows-01	6.0	20.8	A-DWN270	0.94	11.9	9.4	0.8
6	645	Whittier, Narrows-01	6.0	24.5	A-OR2010	0.23	7.1	7.6	0.8
6	652	Whittier, Narrows-01	6.0	26.7	A-DEL000	0.28	8.9	7.2	0.7
7	732	Loma Prieta	6.9	43.2	A02043	0.09	5.0	5.0	1.1
7	771	Loma Prieta	6.9	79.8	GGB270	0.14	5.7	4.5	1.2
7	787	Loma Prieta	6.9	30.9	SLC270	0.11	4.6	3.7	1.3
7	796	Loma Prieta	6.9	77.4	PRS090	0.18	6.0	5.2	1.1
7	802	Loma Prieta	6.9	8.5	STG090	0.15	7.0	2.0	3.5
8	825	Cape Mendocino	7.0	7.0	CPM000	0.10	11.9	6.9	2.4
9	879	Landers	7.3	2.2	LCN260	0.04	5.3	1.3	5.1
10	953	Northridge-01	6.7	17.2	MUL009	0.12	7.3	4.9	1.1
10	983	Northridge-01	6.7	5.4	JGB022	0.10	7.4	3.0	2.9
10	1003	Northridge-01	6.7	27.0	STN020	0.33	12.2	8.2	0.6
10	1045	Northridge-01	6.7	5.5	WPI046	0.03	3.5	2.8	1.8
10	1045	Northridge-01	6.7	5.5	WPI316	0.10	5.9	4.2	1.4
10	1050	Northridge-01	6.7	7.0	PAC175	0.20	9.1	8.9	0.5
10	1054	Northridge-01	6.7	7.5	PAR--L	0.09	7.2	5.7	1.0
10	1063	Northridge-01	6.7	6.5	RRS228	0.04	5.8	5.9	1.1
10	1085	Northridge-01	6.7	5.2	SCE281	0.12	7.3	4.7	1.3
10	1086	Northridge-01	6.7	5.3	SYL090	0.10	7.6	4.4	1.9
11	1148	Kocaeli, Turkey	7.5	13.5	ARE000	1.06	14.8	3.3	4.6
11	1148	Kocaeli, Turkey	7.5	13.5	ARE090	0.08	3.3	0.9	4.1
11	1165	Kocaeli, Turkey	7.5	7.2	IZT090	0.15	5.9	2.3	3.9
12	1182	Chi-Chi, Taiwan	7.6	9.8	CHY006-W	0.10	5.8	3.1	1.8
12	1473	Chi-Chi, Taiwan	7.6	66.3	TCU018-N	0.10	2.4	1.2	5.5
12	1475	Chi-Chi, Taiwan	7.6	56.1	TCU026-E	0.08	3.1	1.0	6.8
12	1480	Chi-Chi, Taiwan	7.6	19.8	TCU036-N	0.05	2.6	1.3	6.3
12	1481	Chi-Chi, Taiwan	7.6	25.4	TCU038-N	0.09	3.6	1.3	6.5
12	1483	Chi-Chi, Taiwan	7.6	22.1	TCU040-E	0.05	2.8	0.9	4.9
12	1489	Chi-Chi, Taiwan	7.6	3.8	TCU049-E	0.10	5.1	1.3	6.3
12	1490	Chi-Chi, Taiwan	7.6	9.5	TCU050-E	0.11	3.9	1.2	6.5
12	1491	Chi-Chi, Taiwan	7.6	7.6	TCU051-E	0.05	2.9	1.2	5.5
12	1492	Chi-Chi, Taiwan	7.6	0.7	TCU052-E	0.02	2.3	1.1	5.7
12	1493	Chi-Chi, Taiwan	7.6	6.0	TCU053-E	0.14	5.7	1.5	4.3
12	1494	Chi-Chi, Taiwan	7.6	5.3	TCU054-E	0.07	3.1	1.0	6.1
12	1496	Chi-Chi, Taiwan	7.6	10.5	TCU056-E	0.08	3.6	1.1	6.5
12	1501	Chi-Chi, Taiwan	7.6	9.8	TCU063-N	0.02	1.6	1.4	4.0
12	1502	Chi-Chi, Taiwan	7.6	16.6	TCU064-N	0.04	2.1	1.0	5.2
12	1504	Chi-Chi, Taiwan	7.6	0.6	TCU067-E	0.06	5.3	2.1	2.2
12	1510	Chi-Chi, Taiwan	7.6	0.9	TCU075-E	0.03	3.0	1.5	3.9
12	1511	Chi-Chi, Taiwan	7.6	2.7	TCU076-E	0.13	6.5	1.9	3.2
12	1515	Chi-Chi, Taiwan	7.6	5.2	TCU082-E	0.07	4.0	1.1	6.2
12	1519	Chi-Chi, Taiwan	7.6	7.0	TCU087-E	0.06	2.7	0.8	5.3
12	1519	Chi-Chi, Taiwan	7.6	7.0	TCU087-N	0.07	2.8	1.5	3.8
12	1520	Chi-Chi, Taiwan	7.6	18.2	TCU088-N	0.43	14.8	3.7	4.9

12	1526	Chi-Chi, Taiwan	7.6	47.7	TCU098-E	0.05	2.3	1.1	8.2
12	1527	Chi-Chi, Taiwan	7.6	11.4	TCU100-E	0.07	2.8	1.0	6.4
12	1528	Chi-Chi, Taiwan	7.6	2.1	TCU101-N	0.10	5.0	1.7	4.4
12	1529	Chi-Chi, Taiwan	7.6	1.5	TCU102-E	0.04	3.3	2.0	2.9
12	1531	Chi-Chi, Taiwan	7.6	12.9	TCU104-E	0.11	3.3	1.1	6.6
12	1548	Chi-Chi, Taiwan	7.6	13.1	TCU128-E	0.03	2.2	1.1	5.5
12	1550	Chi-Chi, Taiwan	7.6	8.3	TCU136-N	0.06	3.3	1.4	3.4
12	1550	Chi-Chi, Taiwan	7.6	8.3	TCU136-W	0.08	3.7	1.3	6.9
13	1605	Duzce, Turkey	7.1	6.6	DZC180	0.08	5.6	2.9	3.8
14	1787	Hector Mine	7.1	11.7	HEC000	0.38	10.0	3.5	5.0
15	3548	Loma Prieta	6.9	5.0	LEX000	0.06	5.1	4.2	1.1
15	3548	Loma Prieta	6.9	5.0	LEX090	0.04	4.2	3.4	1.2
16	3744	Cape Mendocino	7.0	12.2	BNH360	0.09	4.2	2.7	1.9
16	3748	Cape Mendocino	7.0	19.3	FFS270	0.05	4.1	3.5	1.4
16	3748	Cape Mendocino	7.0	19.3	FFS360	0.10	5.0	4.2	1.0
16	3749	Cape Mendocino	7.0	20.4	FFT270	0.28	9.6	4.2	2.9
16	3750	Cape Mendocino	7.0	25.9	LFS360	0.28	8.5	3.6	5.1
17	3947	Tottori, Japan	6.6	5.9	SMNH01EW	0.48	17.1	4.7	3.7
17	3968	Tottori, Japan	6.6	1.0	TTRH02NS	0.06	7.5	4.9	0.8
18	4031	San Simeon, CA	6.5	6.2	36695090	0.28	10.9	4.9	2.4
19	4040	Bam, Iran	6.6	1.7	BAM-L	0.05	6.4	3.9	1.5
19	4040	Bam, Iran	6.6	1.7	BAM-T	0.17	10.2	5.3	1.5
20	4097	Parkfield-02, CA	6.0	3.0	SCN360	0.12	6.4	6.7	0.8
20	4098	Parkfield-02, CA	6.0	3.0	C01090	0.27	10.8	6.9	1.3
20	4098	Parkfield-02, CA	6.0	3.0	C01360	0.23	9.0	8.5	1.1
20	4100	Parkfield-02, CA	6.0	3.0	C02090	0.15	9.6	6.8	0.7
20	4100	Parkfield-02, CA	6.0	3.0	C02360	0.18	8.2	8.0	0.8
20	4102	Parkfield-02, CA	6.0	3.6	C03090	0.38	11.1	8.6	0.7
20	4102	Parkfield-02, CA	6.0	3.6	C03360	0.40	15.0	9.6	0.8
20	4103	Parkfield-02, CA	6.0	4.2	C04090	0.54	17.5	12.7	0.6
20	4103	Parkfield-02, CA	6.0	4.2	C04360	0.70	18.8	13.5	0.5
20	4107	Parkfield-02, CA	6.0	2.5	COW360	0.12	10.0	6.5	1.0
20	4115	Parkfield-02, CA	6.0	2.7	PRK360	0.14	6.4	4.9	1.1
20	4116	Parkfield-02, CA	6.0	8.8	Z14090	0.18	15.4	9.9	0.7
20	4116	Parkfield-02, CA	6.0	8.8	Z14360	0.32	13.3	7.8	0.7
20	4126	Parkfield-02, CA	6.0	3.8	SC1090	0.52	18.6	12.5	0.8
20	4126	Parkfield-02, CA	6.0	3.8	SC1360	0.51	20.5	13.4	0.4
21	4228	Niigata, Japan	6.6	8.9	NIGH11EW	0.17	10.1	7.5	0.8
22	4480	L'Aquila, Italy	6.3	6.3	GX066XTE	0.40	16.1	7.6	0.8
23	4847	Chuetsu-oki, Japan	6.8	11.9	65010EW	0.06	5.0	4.6	1.4
23	4847	Chuetsu-oki, Japan	6.8	11.9	65010NS	0.12	6.1	3.3	2.3
23	4850	Chuetsu-oki, Japan	6.8	16.9	65013NS	0.11	5.9	4.9	1.7
23	4856	Chuetsu-oki, Japan	6.8	11.1	65025EW	0.07	6.7	3.5	2.3
23	4875	Chuetsu-oki, Japan	6.8	12.0	65058EW	0.03	3.4	2.6	2.4
23	4879	Chuetsu-oki, Japan	6.8	19.0	65084EW	0.18	6.2	6.0	1.2
23	4896	Chuetsu-oki, Japan	6.8	11.0	SG01EW	0.03	3.5	2.6	2.4
23	4896	Chuetsu-oki, Japan	6.8	11.0	SG01NS	0.04	3.8	3.4	1.6
24	5658	Iwate, Japan	6.9	6.0	IWTH26NS	0.26	15.2	4.6	1.6
24	5663	Iwate, Japan	6.9	20.2	MYG004NS	0.36	16.2	3.9	3.9
25	5810	Darfield, New Zealand	6.9	24.1	56362EW	0.10	4.0	1.6	4.0
25	6889	Darfield, New Zealand	7.0	18.4	CHHCN01W	0.05	3.1	1.7	4.6
25	6897	Darfield, New Zealand	7.0	8.5	DSLCN27W	0.16	6.4	1.7	6.0
25	6897	Darfield, New Zealand	7.0	8.5	DSLCN63E	0.05	3.5	1.1	5.4
25	6911	Darfield, New Zealand	7.0	7.3	HORCN18E	0.04	4.2	2.5	2.5
25	6915	Darfield, New Zealand	7.0	24.5	HVSCS26W	0.32	13.4	4.0	3.4
25	6928	Darfield, New Zealand	7.0	25.7	LPCCS10E	0.38	11.5	2.7	5.5
25	6953	Darfield, New Zealand	7.0	24.6	PRPCW	0.22	6.6	2.7	3.7
25	6975	Darfield, New Zealand	7.0	6.1	TPLCN27W	0.05	3.9	0.9	7.6
25	6975	Darfield, New Zealand	7.0	6.1	TPLCS63W	0.10	4.5	1.1	5.8
26	8124	Christchurch, New Zealand	6.2	9.4	RHSCN86W	0.25	8.4	3.7	2.1
26	8134	Christchurch, New Zealand	6.2	11.3	SMTCN88W	0.14	5.1	3.2	1.1
26	8158	Christchurch, New Zealand	6.2	6.1	LPCCN10W	0.55	22.1	7.0	1.6
27	8164	Duzce, Turkey	7.1	2.7	487-NS	0.20	7.6	2.9	5.2
28	8606	EI Mayor-Cucapah	7.2	11.4	CIWESHNN	0.08	4.5	1.4	6.6

